The accumulation and dispersion of heavy particles in forced two-dimensional mixing layers. I. The fundamental and subharmonic cases

J. E. Martin[a] and E. Meiburg
Department of Aerospace Engineering, University of Southern California, Los Angeles, California 90089-1191

This paper presents detailed computational results for the dispersion of heavy particles in transitional mixing layers forced at both the fundamental and subharmonic frequencies. The results confirm earlier observations of particle streaks forming in the braid region between successive vortices. A scaling argument based on the idealization of the spatially periodic mixing layer as a row of point vortices shows that the formation of these concentrated particle streaks proceeds with optimum efficiency for $St \approx 1$. It thereby provides a quantitative basis for experimental and numerical observations of preferential particle dispersion at Stokes numbers of order unity. Both the model and full simulation furthermore exhibit oscillatory particle motion, as well as the formation of two bands of high particle concentrations, for larger Stokes numbers. The particle dispersion as a function of time and the Stokes number is quantified by means of two different integral scales. These show that the number of dispersed particles does not reach a maximum for intermediate Stokes number. However, when the distance is weighted, optimum dispersion is observed for Stokes numbers around unity. By tracing the dispersed particles backwards in time, they are found to originate in inclined, narrow bands that initially stretch from the braid region into the seeded free stream. This suggests that particle dispersion can be optimized by phase coupling the injection device with the forcing signal for the continuous phase. In the presence of a subharmonic perturbation, enhanced particle dispersion is observed as a result of the motion of the vortices, whereby a larger part of the flow field is swept out.

I. INTRODUCTION

The transport of small solid particles or droplets represents a characteristic feature of numerous fluid flows in both nature as well as technical applications. The latter category is exemplified by condensation phenomena in the final stages of large turbines and by spray combustion, which are issues that recently have been the focus of much attention. On the other hand, the convective transport and settling of a particulate or droplet phase in the atmosphere, or in lakes, rivers, and the oceans is of importance for understanding natural climatic processes and for assessing the impact of human activities on the environment.

Much of the established knowledge base on the dispersion of particles in fluid flows is due to classical analytical considerations. In recent years, the rapid advances in both experimental and computational capabilities have allowed us to gain deeper insight into the governing mechanisms and to arrive at a more detailed understanding of the important phenomena. However, for problems involving many particles even today's supercomputers do not yet permit the explicit computation of the detailed mass, momentum, and energy exchanges between the two phases. Consequently, most numerical studies so far have focused on systems in which the mass and volume fractions of the particulate phase are small enough so that their effect on the fluid phase can safely be neglected. However, some progress has been made recently in taking into account the effect of the dispersed phase onto the continuous phase by

means of a force term in the Navier–Stokes equations, cf. Squires and Eaton.[1] For dilute suspensions, computational investigations have provided considerable insight into the mechanisms that govern the evolution of the particle concentration field. A most interesting finding was reported by Crowe, Gore, and Troutt,[2] who analyzed the influence of the large scale structures in turbulent free shear flows on the dispersion of the particular phase. Their two-dimensional vortex dynamics simulations use a low-order time integration scheme to create numerical fluctuations that are supposed to mimic a turbulent velocity field. These calculations demonstrate the tendency of very small particles to closely follow the fluid elements, as the dominant Stokes drag force dictates their dynamics. Very heavy particles, on the other hand, possess large inertia, and their trajectories hardly change under the influence of the forces exerted upon them by the fluid. However, for intermediate particle sizes, the authors observe a fairly strong dispersion, which can even exceed that of the fluid particles. Here the quantitative comparison between fluid element and particle dispersion is based on a definition of the dispersion function which depends on the initial particle location, so that it is somewhat difficult to extract information on the global dispersion of particles. However, the computations clearly identify as the driving mechanism for this strong dispersion the large scale coherent vortical structures,[3,4] which dominate the turbulent mixing layer and eject particles into the free stream. This mechanism is most effective when the aerodynamic response time of the particles is of the same magnitude as the characteristic flow time associated with the coherent structures. Chung and Troutt[5] dem-

onstrated the same effect in axisymmetric jets, while Chein and Chung[6] observed that vortex pairing events result in even higher lateral dispersion rates. A recent review of these and other results is given by Crowe, Chung, and Troutt.[7]

The optimal dispersion of intermediate particle sizes is confirmed by the detailed experimental investigations of Lázaro and Lasheras,[8–10] which provide a wealth of information regarding natural and forced plane turbulent mixing layers. Their measurements clearly demonstrate the selective dispersion of particles of different sizes. Furthermore, both experiments and scaling arguments indicate that the maximum droplet size affected by the layer grows as the square root of the streamwise distance. For unforced flows (Lázaro and Lasheras[9]), the authors observe that all particle sizes disperse at a smaller rate than the fluid momentum, whereas if they apply forcing at the first subharmonic of the most unstable frequency (Lázaro and Lasheras[10]), the particle dispersion can exceed that of the streamwise momentum of the carrier gas. These authors quantify the particle dispersion in terms of a concentration level thickness. By scaling the flow-field coordinates appropriately, they are able to show, for the unforced case, the existence of a universal dispersion law that is particle size independent. For the forced flow, such a general relationship does not exist. Kiger and Lasheras[11] observe that, in the presence of a vortex pairing event, the concentration and particle size distribution profiles are considerably more homogeneous across the mixing layer than for fundamental wave forcing only.

Both the numerical simulations and the flow visualization experiments mentioned above demonstrate the importance of large scale particle streaks, which were also observed in the experiments of Longmire and Eaton[12] as well as in the numerical and experimental investigation of Wen et al.[13] These streaks form in the braid region between consecutive vortices and appear to dominate the cross-stream dispersion.

Further insight into the dynamics of heavy particles in a plane mixing layer can be gained by numerically analyzing the motion of individual particles in idealized representations of the flow field. This route was taken by Gañán-Calvo and Lasheras,[14] who applied a nonlinear dynamical systems approach in studying the behavior of particles in a row of Stuart vortices[15] under gravity. The authors observe that if gravity is of moderate importance, the particles can stay suspended above the mixing layer. In this case, the particle trajectories can be periodic, quasiperiodic, or chaotic. If gravity is more dominant, the particles sediment. The above investigation has been extended by Tio et al.,[16] who find suspension of heavy particles both above and below the mixing layer vortices. A more detailed understanding of the relevant mechanisms can be obtained from the perturbation analyses of Tio et al.[17] and Tio and Lasheras.[18]

The present investigation aims at further elucidating the particle dispersion mechanisms in free-shear layers by means of detailed numerical simulations in the dilute regime. By dealing with nonturbulent flows, we will be able to study the relevant mechanisms for clean flow structures, without the superimposed fluctuations due to turbulence. This approach should be helpful in the development of a structure-based particle dispersion model. In particular, we will investigate the formation and evolution of the particle streaks, in order to assess their overall importance. This will aid us in putting forward a quantitative argument for the optimum dispersion of intermediate size particles, based on an idealization of the two-dimensional mixing layer and in particular, the region near the free-stagnation points. We will furthermore focus on the role of subharmonic perturbations for the dispersion of particles. In order to quantify the global dispersion efficiency of the various flow fields, we will compare integral length scales that reflect both the number of dispersed particles as well as the distance over which they are dispersed.

Similar to previous authors, we assume the dilute suspension limit, i.e., we study the dynamics of the particles under the influence of the fluid flow, without considering any feedback to the flow. The governing equations are stated in Sec. II. Section III presents results for mixing layers perturbed by a fundamental wave only, as well as by an additional subharmonic wave. Our findings will be summarized and some conclusions will be drawn in Sec. IV. The present study is the first part of a more comprehensive investigation, with Part II (Raju and Meiburg[19]) focusing on the effect of gravity and its nonlinear interaction with the mechanisms described here.

II. NUMERICAL APPROACH

A. Simulation of flow field

Our goal is to study the spatio-temporal evolution of the particle concentration field in response to the forcing provided by the large scale structures of the growing shear layer. In this investigation, we limit ourselves to the dilute regime of particle concentration, in which the evolution of the continuous fluid phase is independent of the particle concentration field. Consequently, we are able to calculate the fluid velocities independently of the particle motion.

Since the generation, growth, and merging of the large-scale mixing layer vortices is dominated by inviscid mechanisms, we employ a two-dimensional vortex dynamics technique for the simulation of Euler's equations. These methods, as reviewed by Leonard,[20] are well established and offer an efficient and conceptually straightforward way to capture all of the large-scale features of evolving free-shear flows. A brief description of the particular variant employed in this study is given in the following. The rotational portion of the fluid is discretized into a row of N vortex blobs of radius σ and circulation Γ_i $(i=1,N)$. The basic assumption that the flow field is inviscid then allows one to make use of the theorems of Kelvin and Helmholtz to advance the blobs as material elements according to the Biot–Savart law,[21] while maintaining their circulation Γ_i as being fixed. We consider the case of a streamwise periodic, temporally evolving mixing layer. This model captures all of the dominant features of a mixing layer, including the instability of the vorticity layer, the formation and subse-

J. E. Martin and E. Meiburg   1117

quent pairing of the large scale spanwise vortices and the inherent strain field. Furthermore, the temporally evolving case is numerically more efficient and it avoids the problem of assigning inflow and outflow boundary conditions. We obtain a smooth vorticity field by employing an invariant vorticity distribution of the form

$$\omega(r) = \Gamma_i/(\pi\sigma^2)\exp(-r^2/\sigma^2)$$

in which r is the radial distance from the blob center. For the calculation of the velocity field, the Biot–Savart law requires integration over the entire vorticity field. Therefore, the far-field effect of the streamwise periodic images of the blobs must also be taken into account. This can be evaluated analytically by treating the images of the vortex blobs as point vortices,[22] so that the overall velocities in the streamwise and cross-stream directions, respectively, are given by

$$u(x,y) = \sum_{i=1}^{N} \left[\frac{1}{2\pi} \frac{y-y_i}{r^2} \Gamma_i \exp\left(-\frac{r^2}{\sigma^2}\right) \right.$$
$$\left. -\frac{\Gamma_i}{2L} \frac{\sinh[2\pi(y-y_i)/L]}{\cosh[2\pi(y-y_i)/L]-\cos[2\pi(x-x_i)/L]} \right],$$

$$v(x,y) = \sum_{i=1}^{N} \left[-\frac{1}{2\pi} \frac{x-x_i}{r^2} \Gamma_i \exp\left(-\frac{r^2}{\sigma^2}\right) \right.$$
$$\left. +\frac{\Gamma_i}{2L} \frac{\sin[2\pi(x-x_i)/L]}{\cosh[2\pi(y-y_i)/L]-\cos[2\pi(x-x_i)/L]} \right]$$

(1)

in which (x_i,y_i) represents the time dependent position of each blob and L is the streamwise dimension of the periodic control volume.

We advance the flow field in time by calculating the velocity induced at the center of each blob $u(x_j,t)$ and by advancing the blobs' positions x_j, according to the equation

$$\frac{dx_j}{dt} = u(x_j,t), \tag{2}$$

where summation in Eq. (1) now takes place for all i not equal to j. A fourth-order accurate Runge–Kutta scheme is used for the time integration of the blob positions. We take the velocity difference between the two streams ΔU as our characteristic velocity. The vorticity thickness δ of the shear layer serves as the characteristic length scale resulting in an initial blob core radius of $\pi^{-1/2}$. To determine the optimal spatial discretization, the number of blobs was increased until no further change in the maximum vorticity occurred during the evolution of the flow. Typically, this resulted in a discretization of 59 blobs per basic wavelength.

In analogy to forcing the flow in an experiment, we initially impose a sinusoidal modification to the strength of the vortex blobs. This perturbation induces the instability and roll-up of the shear layer. It is given by

$$\Gamma_i = \Gamma_{i0}(1+0.05\sin\alpha x),$$

where Γ_{i0} is the vortex blob strength corresponding to the unperturbed flow. The wave number α of the fundamental perturbation in all cases is chosen based on the inviscid stability analysis of Michalke[23] ($\alpha=2\pi/L=0.8892$). For cases involving pairing, an additional equal amplitude, subharmonic perturbation is imposed. The subharmonic perturbation is of the same amplitude as the basic wave, while its phase is chosen such that the maximum occurs halfway between the evolving vortices. In this way, the subharmonic wave will induce a vortex pairing process.

B. Particle equation

We consider particles whose density ρ_p is much greater than that of the surrounding fluid. The particles, whose effect upon each other is neglected due to the assumption of a dilute suspension, are assumed to remain spherical throughout the evolution of the flow. For these conditions, the equation governing the velocity $v_p(t)$ of the particle in a nonuniform flow field $u(x,t)$ was derived by Maxey and Riley[24]

$$V\rho_p \frac{dv_p}{dt} = 6\pi a\mu [u(x,t)|_{x=x_p(t)} - v_p(t)] + V(\rho_p-\rho_f)g + V\rho_f \frac{Du}{Dt}\bigg|_{x=x_p(t)} + \frac{1}{2} V\rho_f \frac{d}{dt}[u(x,t)|_{x=x_p(t)} - v_p(t)]$$

$$-6\pi a^2\mu \int_0^t \left(\frac{(d/d\tau)\,[v_p(\tau)-u(x,t)|_{x=x_p(t)}]}{[\pi\mu(t-\tau)/\rho_f]^{1/2}} \right) d\tau.$$

In the above equation, we neglect the Faxen correction terms, which become significant only in the event of large curvature in the velocity profile. Here ρ_f and μ are the density and dynamical viscosity of the surrounding fluid, while d_p, V, and $x_p(t)$ represent the diameter, volume, and position of the particle, respectively. The different terms of this equation represent in order, the force needed to accelerate the particle, viscous Stokes drag, gravity, a pressure gradient force accounting for the acceleration of the displaced fluid and the virtual mass and Basset history terms.

The order-of-magnitude estimates presented by Lázaro and Lasheras[8] indicate that, for small heavy particles in the dilute regime, drag, and inertia effects dominate over those of the pressure field, the virtual mass, and the particle's history. Consequently, within the present investigation, we retain only the terms describing inertia, drag, and gravity. In dimensionless form, the governing equation for the evolution of the particle's velocity then becomes

$$\frac{d\mathbf{v}_p}{dt} = \frac{1}{\mathrm{St}}\left[\mathbf{u}(\mathbf{x},t)\big|_{\mathbf{x}=\mathbf{x}_p(t)} - \mathbf{v}_p(t)\right] - \frac{1}{\mathrm{Fr}^2}\mathbf{e}_g, \qquad (3)$$

where

$$\mathrm{St} = \frac{\rho_p d_p^2}{18\mu} \cdot \frac{\Delta U}{\delta}, \quad \mathrm{Fr} = \frac{\Delta U}{\sqrt{\delta g}}.$$

Gravity has the magnitude g and acts in the direction $\mathbf{e}_g$, which can be parallel or perpendicular to the direction of the free stream. Within Part I of the present investigation, we do not consider the effect of gravity, i.e., Fr is infinitely large. Part II will present a detailed discussion of the effect of gravity. The Stokes number St expresses the relative importance of particle inertia to viscous drag. It can also be interpreted as the ratio of the particle's aerodynamic response time to the characteristic flow time.[2] Fr denotes the Froude number and indicates the relative importance of inertial forces and gravity. It should be mentioned that by applying Stokes's drag law, we tacitly assume that the particle Reynolds number

$$\mathrm{Re}_p = \rho_p |\mathbf{u} - \mathbf{v}_p| d_p / \mu$$

is small. Equation (3) together with

$$\frac{d\mathbf{x}_p}{dt} = \mathbf{v}_p(t) \qquad (4)$$

then govern the particle motion. We integrate in time by using the same fourth-order Runge–Kutta scheme as for the continuous phase. For particles of small Stokes number, the time step is restricted so that $\Delta t/\mathrm{St} < 2.0$ to avoid numerical instabilities in the calculation of the particle motion. In order to establish initial conditions for the particle velocity, we assume the particle to be in equilibrium with the fluid. Consequently, we assign the particle a velocity equal to the fluid velocity at the particle's position.

C. Interpolation scheme

Central to the particle acceleration equation (3) is the evaluation of the fluid velocity at the particle position, i.e., $\mathbf{u}[\mathbf{x}=\mathbf{x}_p(t),t]$. For each particle at each time step, the direct summation of Eq. (1) over all vortex blobs must then be calculated. However, since it is necessary to include as many as 10^6 particles in a calculation to obtain accurate statistics, this direct summation becomes prohibitively expensive. A more economical approach is to use Eq. (1) to evaluate the fluid velocities on a fixed grid of points. The fluid velocities at the particle positions can then be obtained by interpolating the grid values. Furthermore, if deemed necessary to improve particle statistics, additional simulations for the same flow field can be then performed without the costly reevaluation of (1).

Different interpolation methods and their accuracies have been discussed in detail by Balachandar and Maxey[25] in the context of spectral simulations of turbulence. For heavy particles undergoing Stokes drag, Browand, Nassef, and Spalart[26] employ interpolation methods in a turbulent boundary layer, as do Squires and Eaton[1] in seeded isotropic turbulence. In general, the use of linear interpolation,

although computationally fast, is inferior to other interpolation methods for use in fluid or particle tracking. Lagrangian interpolation methods are superior in accuracy over other methods while suffering from very little additional computational effort.[25]

In this study, we will use a fourth-order, two-dimensional Lagrangian interpolation scheme. Fluid velocities on the 4×4 lattice of grid locations surrounding the particle are used in the evaluation of the velocity at the particle location. The interpolated particle velocity $\mathbf{u}_I$ is then given by

$$\mathbf{u}_I(x,y,t) = \sum_{i=0}^{3} \sum_{j=0}^{3} \mathbf{u}(x_i,y_j,t) L_i(x) L_j(y),$$

where the x_i and y_j are the surrounding grid points. The basis function L_i is given by

$$L_i(x) = \prod_{\substack{k=0 \\ k \neq i}}^{3} \frac{(x-x_k)}{x_i - x_k}$$

and similarly for $L_j(y)$. Thus, in each direction, $\mathbf{u}_I$ is a polynomial of degree three which coincides identically with the value of the fluid velocity at each lattice point. As the maximum spacing h between grid points goes to zero, the error of this approximation decreases as $O(h^4)$.[27]

To determine the error incurred with the use of interpolation, we run one calculation in which the particle velocities are calculated by interpolation and compare with a calculation with identical initial conditions, where particle velocities are calculated explicitly. We compute the maximum difference between the two locations calculated for each particle at time $t=21.0$, by which time the shear layer perturbation has grown well into the nonlinear regime. Figure 1 shows the results for Stokes numbers of 10^2 and 1.0 using both Lagrangian and linear interpolation. We recognize the fourth-order accuracy of the Lagrangian scheme, whereas the linear scheme is only second-order accurate in space. Furthermore, it is obvious that the error can be kept quite small even with a moderate number of grid points. We hence conclude that Lagrangian interpolation can provide significant savings with a minimal loss of accuracy. For each calculation, we use an interpolation grid with $h < 0.1414$ resulting in a maximum error in particle position at time $t=21.0$ of less than 10^{-2}.

III. RESULTS

A. Physical effects governing particle dispersion in plane mixing layers without gravity

Here we consider the evolution of the particle field in the absence of gravity. The mixing layer is perturbed by a fundamental wave only. We initially seed the upper stream of the mixing layer by randomly distributing 100 000 particles over the streamwise wavelength between $y=0$ and $y=4$. Once the initial conditions are set, the sole parameter governing the particles' dynamics is the Stokes number. In the following, we will discuss a series of simulations performed for Stokes numbers between 10^{-2} and 10^2.
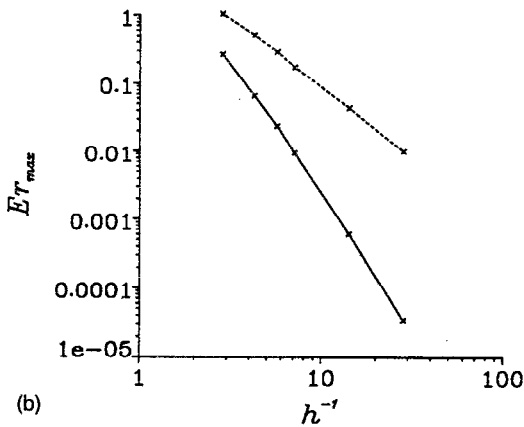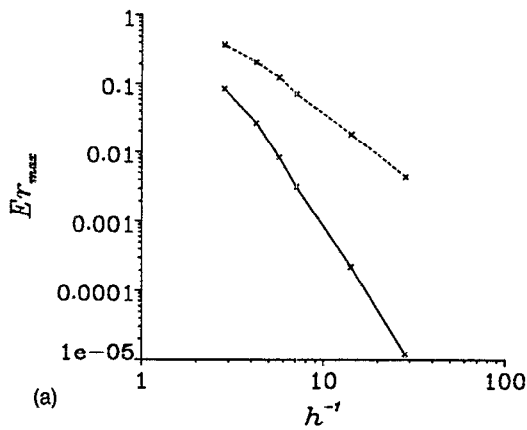
(a)

(b)

FIG. 1. Maximum error in particle position incurred by interpolating fluid velocities at particle positions, $t=21.0$: (a) $St=10^2$, (b) $St=1.0$.———: Lagrangian interpolation; - - -: linear interpolation.
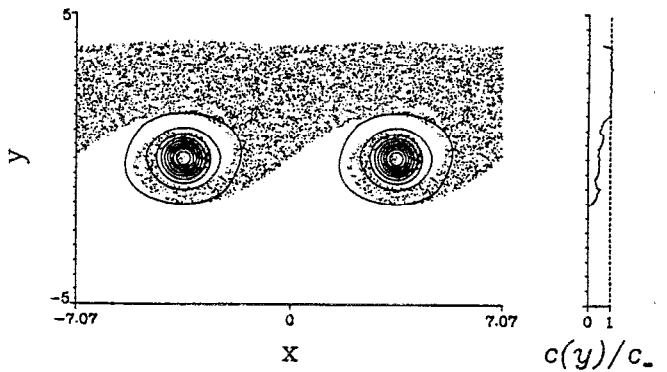

FIG. 2. Vorticity contours with particle positions superimposed for $St=10^{-2}$ at time $t=18.0$. Two streamwise wavelengths are displayed. On the right is the corresponding streamwise-averaged, particle concentration profile. Particle inertia is small, or alternatively viscous drag large, forcing particles to closely follow the motion of the fluid throughout the evolution of the flow.

Figure 2 shows the flow field at times $t=18$ for a Stokes number 10^{-2} simulation. The locations for 4200 of the 100 000 particles are plotted, along with the vorticity contours at the corresponding times, which illustrate the fluid phase evolution. The contour levels are at 10% increments of the maximum vorticity occurring during the evolution of the flow up to time 30. To the right of each particle location plot, we include the corresponding streamwise-averaged particle concentration profile, $c(y)$. We will later use these profiles to quantify the dispersion rates for the different particle Stokes numbers. To attain the particle concentration $c(y)$, we divide the cross-stream distance into bins (height $\Delta y=0.05$) which extend over the streamwise wavelength L. We then count particles residing within each bin to give us the value $c(y)$ over the distance Δy. We nondimensionalize $c(y)$ by a reference level c_∞, where c_∞ is the uniform particle concentration in the free stream seeded with particles. During the initial growth of the Kelvin–Helmholtz instability, the averaged particle concentration profile $c(y)$ maintains a steep gradient across the interface. For this small Stokes number, viscous drag can be expected to dominate over inertia effects. Consequently, the particle motion mirrors that of material fluid elements, and particles are convected around the emerging vortices, which are connected by braid re-
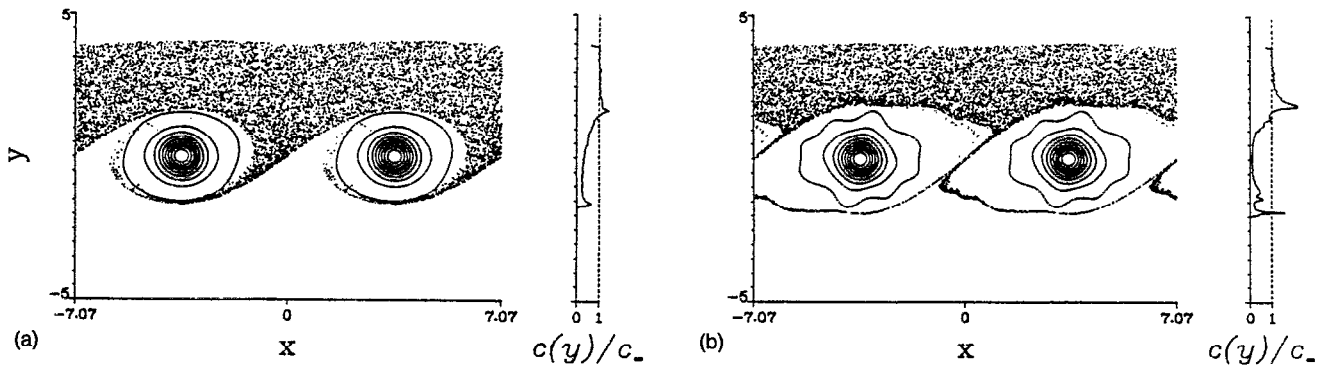

(a)

(b)

FIG. 3. Vorticity contours with particle positions superimposed for $St=1.0$ at times (a) $t=18.0$ and (b) $t=30.0$. Two streamwise wavelengths are displayed. On the right is the corresponding streamwise-averaged particle concentration profile. Particles for St $O(1)$ are centrifuged from the large-scale vortices (Crowe et al.[2]). By time 18.0, streaks of particles cross far into the unseeded stream. Sharp spikes in the particle concentration profile indicate the particles' strong preferential residence along the stagnation streamline of the flow field.
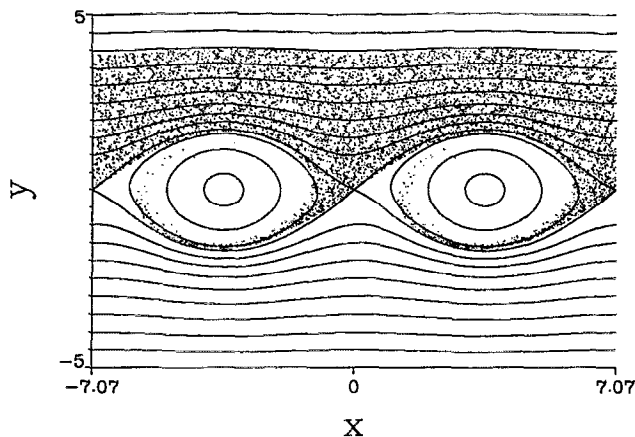
J. E. Martin and E. Meiburg

FIG. 4. Streamlines, with particle positions superimposed, for St = 1.0 at time $t=18.0$. The stagnation streamline approximately forms a lower border for the particle streaks at this time.

FIG. 5. Overall particle concentration, as indicated by grey-scale shading for St = 1.0 at time $t=18$. Maximum particle accumulation occurs in a thin band extending through the stagnation point. The stretching of this band is responsible for the formation of the particle streaks and enhances particle dispersion at St of $O(1)$.

gions that become depleted of vorticity. By time of $t=18$, the flow field is dominated by the vortices. The particles now form a clear spiral within each vortex, and we observe the continuous growth of a plateau region in the concentration profile.

For simulations with Stokes numbers between 10^{-2} and 10^{-1}, the overall patterns of particle distribution remain similar to those described above for the St = 10^{-2} case. However, as we approach Stokes numbers of order unity, qualitative changes occur. Figure 3 shows our results for the case of St = 1.0 and $t=18$. Most notable is the absence of particles from the regions of the flowfield occupied by the large scale vortices. This is due to the centrifugal effect of the vortices observed by Crowe, Gore, and Troutt[2] as well as others numerically and by Lázaro and Lasheras[8-10] experimentally. It is also reflected in the averaged concentration profile, in which the plateau region is not as well defined as before. This profile is indicative of the increased lateral dispersion of particles which takes place for St = 1.0. It contains many of the characteristics of the polydisperse particle concentration profiles of the experiments by Lázaro and Lasheras,[10] cf. their Fig. 8(a). Our computed particle concentration is nearly constant in the seeded far field. However, at a cross-stream location just above the vortices, the particle concentration reaches a value in excess of the reference level. A similar trend is seen in the overall particle concentration results of the Lázaro and Lasheras experiment. There, as one moves from the core of the spray toward the unseeded stream, a region exists where particle concentration exceeds the seeded, free stream value. A well-defined band of particles emerging from the braid region surrounds the lower perimeter of each vortex. By plotting the instantaneous streamlines along with the particle locations (Fig. 4), we recognize that the evolving streak is approximately aligned with the separating streamline emerging from the free-stagnation point. It hence appears that the deformation field associated with the local neighborhood of the stagnation point is important for the formation of the particle streaks, a point
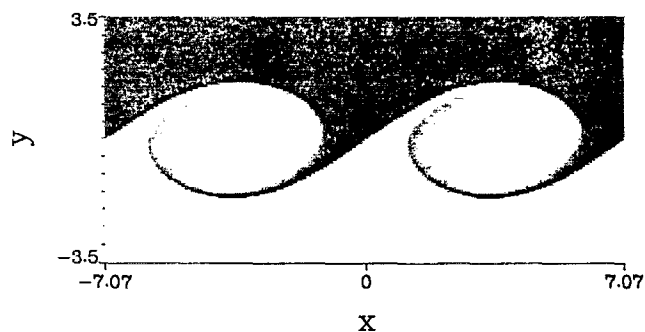
that will be discussed in more detail below. The lower spike in the concentration profile is due to the band of particles below the vortices. Although the profile gives only an average over the streamwise wavelength, it indicates regions in the flow field of strong preferential particle location. By time $t=30$, the band of particles surrounding the vortices forms a closed loop. Near the free stagnation points, the particle bands tend to develop a slight waviness, which resembles the initial stages of lobe formation observed in the calculations of Rom-Kedar et al.[28] and Meiburg et al.[29] for passive particles in time-periodic flow fields. This indicates the potentially important role played by the unstable manifold even for the mixing of heavy particles.

Lázaro and Lasheras[10] observe similar coherent tongue-shaped structures of the particle concentration field, which are located in the braid regions. Although their flow field is polydisperse, these streaks are composed mainly of larger droplets which correspond to the particles of increased Stokes number considered in the present study. The areas near the vortex centers, on the other hand, contain only droplets of very small diameter which correspond to the particles of very small Stokes number discussed above. Streaks of particles in the braid region were furthermore observed by Longmire and Eaton,[12] as well as by Wen et al.[13] The measurements by Lázaro and Lasheras furthermore indicate an overshoot in the concentration profile near the edge of the core, in a fashion similar to the spikes in our computational profiles discussed above.

In order to obtain more detailed information about the accumulation of particles in certain regions, we examine the two-dimensional particle concentration field more closely. For this purpose, we divide our control volume into 114 by 112 rectangular bins and count the particles within each of these. In Fig. 5 we show the overall particle concentration at time $t=18$ in the St = 1.0 simulation. The particle concentration is indicated by a grey-scale shading with black denoting an area of maximum particle concentration. Figure 5 exhibits heavy particle accumulation in a thin band extending through the stagnation point of the flow. This band is aligned with the extensional direction of the strain field, and the particles it contains are accelerated
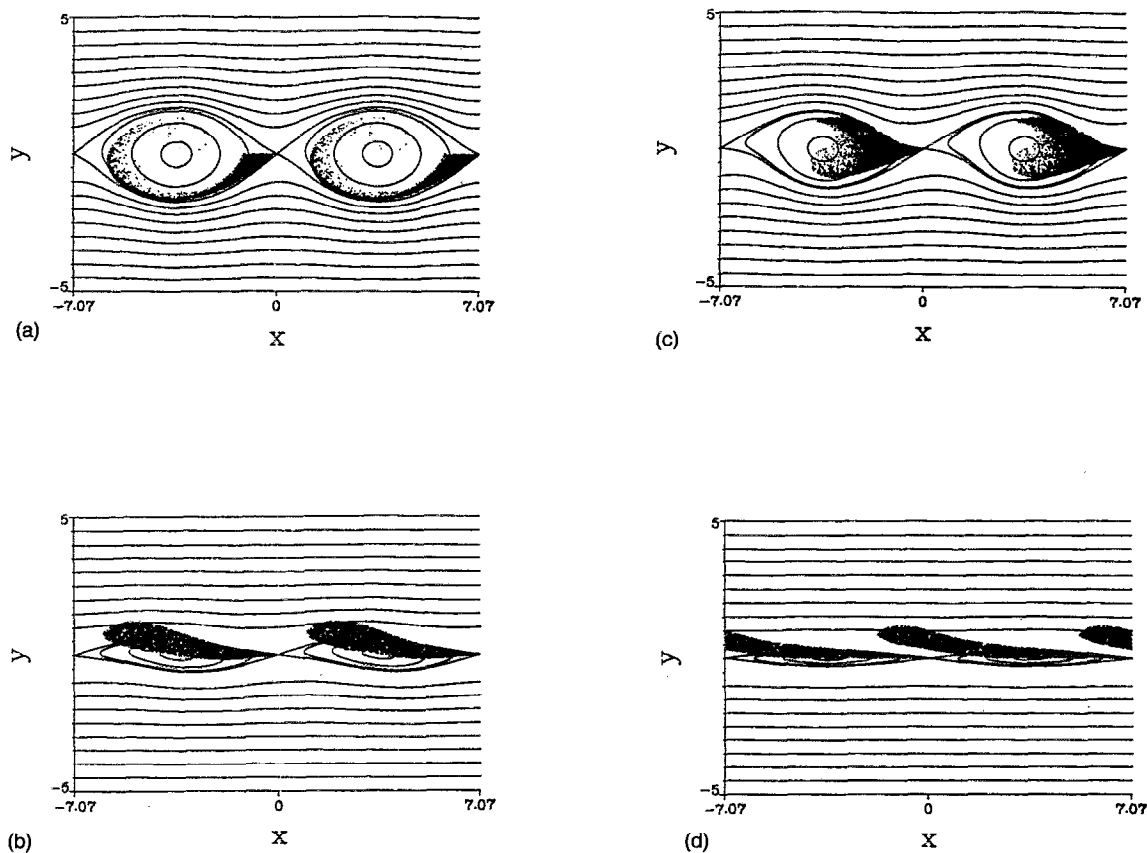
FIG. 6. Backwards (in time) evolution of those particles which ultimately compose tongue-like particle streaks. These are superimposed upon the streamlines of the continuous phase at the corresponding times of (a) $t=18.0$, (b) $t=12.0$, (c) $t=6.0$, and (d) $t=0.0$.

away from the free-stagnation point in this direction. In this way, large numbers of particles are propelled into the lower stream. The accumulation of the particles in this band, and its subsequent stretching into the lower stream, is the main mechanism responsible for the formation of the particle streaks. In Sec. III A 3, we will present a scaling argument for why this process has optimum efficiency for $St \simeq 1$, i.e., why particles of Stokes number $O(1)$ experience maximum dispersion.

The above information confirms the observations of previous investigators about the crucial role played by the particle streaks for enhancing lateral dispersion. Since those particles that accumulate in the bands will be preferentially ejected into the opposite stream, information on where these particles originated will be helpful for designing optimized injection strategies for maximum particle dispersion. In our numerical simulations, this information is of course easily accessible. In Fig. 6(a), we plot only those particles that have crossed the mixing layer centerline by time $t=18$. The instantaneous streamlines of the flow at the corresponding time are superimposed. Figures 6(b)–6(d) then show the locations of these particles at earlier times. We recognize that they originate in fairly thick and slightly curved bands that emanate from the free-stagnation points and extend into the upper stream. It would then appear possible to enhance particle dispersion in an experiment by phase coupling the particle injection device with the forcing signal for the continuous fluid phase. This result corresponds to the findings of Wang[30] for passive fluid particles.

In Fig. 7(a), we display the particle location plot and corresponding streamwise-averaged particle concentration profile for the intermediate time of $t=18$ in a $St=10$ simulation. As pointed out by Crowe, Gore, and Troutt,[2] increasing the Stokes number corresponds to an increase in the particle response time. By increasing the Stokes number, the large-scale vortices have comparatively less time to influence the motion of the particles. The absence of particles from the area near the vortex centers at time $t=18$ thus becomes less pronounced in the $St=10$ case, as the influence of the vortices on the particles is reduced. However, a streak of particles still protrudes from between successive vortices and extends well below the vortices. The particle concentration profile contains a clear spike above the vortices, indicating an accumulation of particles in this region. The cause of this spike becomes obvious from a plot of the overall particle concentration [Fig. 7(b)]. A narrow region of increased particle accumulation extends through the braid region of the flow. The inclination of this line with respect to the centerline of the mixing layer is slightly less than for the $St=1.0$ case. Again, the region of maximum particle concentration begins above the periphery of a vortex, extends through the braid region, and finally forms the tail of a streak of particles reaching below the
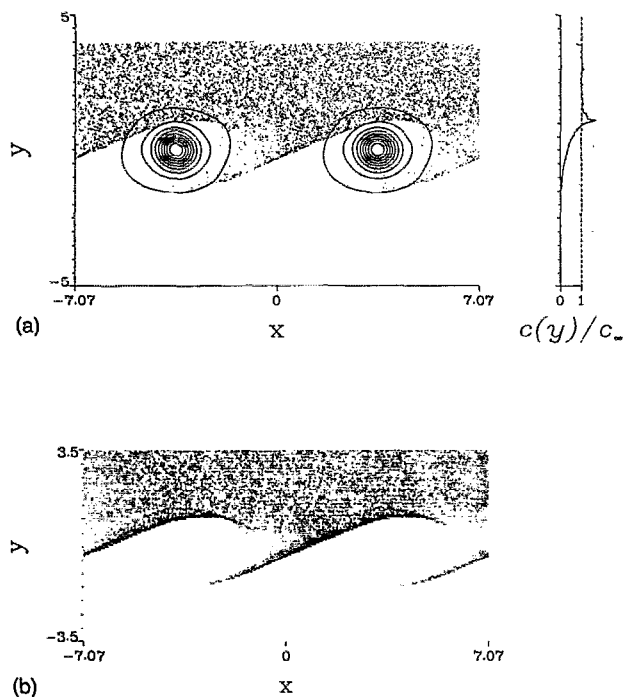
J. E. Martin and E. Meiburg

FIG. 7. (a) Vorticity contours with particle positions superimposed for St=10.0, t=18.0. On the right is the corresponding streamwise-averaged, particle concentration profile. As in the St=1.0 simulation, a particle streak (of somewhat lesser extent than for St=1.0) protrudes from the braid region. The preferential residence of particles in isolated regions of the flow field is indicated by the large spike in the particle concentration profile. (b) The overall particle concentration indicates a band of higher particle accumulation extending through the braid region.

FIG. 8. (a) Vorticity contours with particle positions superimposed for St=100.0, t=18.0. On the right is the corresponding streamwise-averaged, particle concentration profile. Influence of the vortices on the particles is markedly reduced for high St. The particle streaks observed in the St=1.0 and St=10.0 simulations are less evident. However, accumulation of particles is again indicated by the spike in the particle concentration profile and the thin band of higher particle concentration in the overall particle concentration field of (b).

upstream successive vortex. The streak is much less curved at its tip. Eventually, however, by a time of t=30, the streak again forms a closed loop.

We now consider the evolution of particles for the largest Stokes number of 10^2 (Fig. 8). For this large Stokes number, the effect of the initial conditions for the particle velocities will be felt much longer than before. Depending on how the particles are seeded in an experiment, our initial conditions, which set the particle velocities equal to the fluid velocities, may or may not mimic the experimental situation. The influence of the vortices is now markedly reduced. Particles pass nearly directly through the core of the large-scale vortices. Streaks of particles protruding into the unseeded stream exist only in rudimentary form. Again a band of accumulated particles extends through the braid region of the flow, leading to a large overshoot in the particle concentration profile. The inclination of the band, in relation to the centerline of the shear layer, is further reduced from its value observed at smaller Stokes numbers.

In order to investigate the long-time effect of the initial conditions for the particle velocities, we carried out a set of simulations for St=10^2 in which we varied these initial conditions. Figure 9(a) shows the resulting distribution of particles when we set the initial particle velocity equal to the average velocity of the free streams, i.e., to zero in our moving reference frame. Assigning the particles initial velocities equal to the unperturbed velocity of the upper free stream markedly changes the resulting distribution of par-
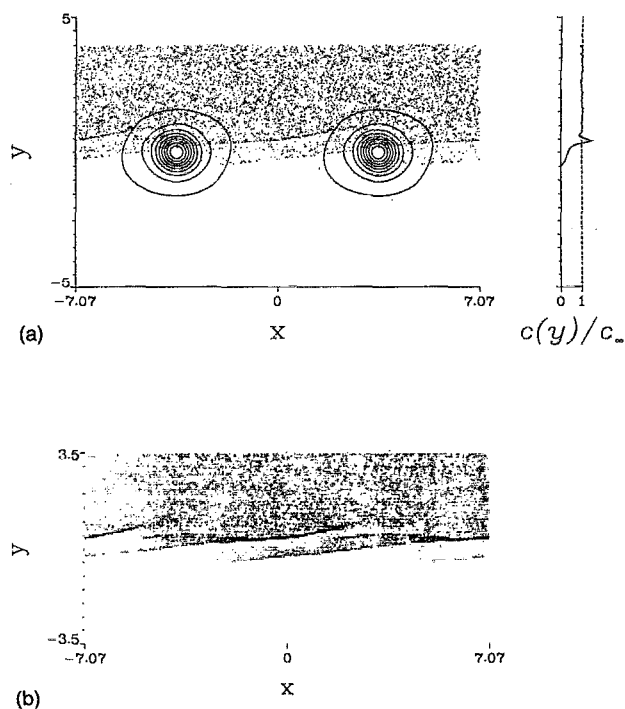
ticles [Fig. 9(b)], which now appears to be largely unaffected by the presence of the vortices. These results are of interest for comparing different methods for seeding the flow with particles of large Stokes number. For instance, by adjusting the direction of particle seeding in the experimental facility, either into the upstream or downstream direction, different initial particle velocities can be produced and different resulting particle distributions can be realized. This leads to the next logical step in the present investigation, namely the quantification of the particle dispersion for the above range of Stokes numbers.

1. Quantification of particle dispersion

Investigations have quantified the particle dispersion mechanisms using different approaches. Batchelor[31] analyzed passive fluid particles in a self-developing turbulent shear flow. A particle dispersion function $D_x(t)$ was used, where

$$[D_x(t)]^2 = \overline{[X(t) - \bar{X}(t)]^2}$$

and $X(t)$ was the particle displacement. The dispersion function for a particle varied in time, proportional to the thickness of the shear layer at the mean position of the particle. Chein and Chung[6,32] in their numerical studies also used $D_x(t)$. They investigated whether a similar interrelation exists in the case of a mixing layer containing the large-scale vortices. The dispersion function was propor-
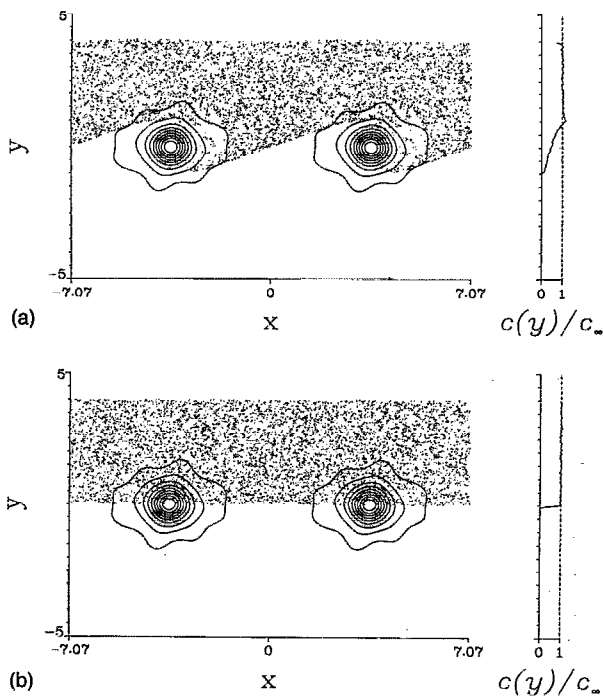
(a)

(b)

FIG. 9. Resulting variation in final particle location for different initial particle velocities in the moving reference frame, $St = 10^2$, $t = 30.0$: (a) $v_p(t=0) = 0.0$. As in Fig. 8, particles again accumulate in a band extending through the braid region. However, the band requires more time to form and has greater inclination than in Fig. 8. (b) $v_p(t=0)$ equal to the free-stream velocity. Influence of the mixing layer upon the particles is markedly reduced. By changing the initial velocity of the seeded particles, the resulting distribution of particles can be varied significantly for very large St.

FIG. 10. Evolution of the 0.9–0.1 particle concentration level thickness for various St. As found in the investigation of Lazaro and Lasheras,[10] δ_L shows the dispersion of intermediate size particles eventually exceeding the dispersion of the surrounding continuous phase. Particles with St of $O(1)$ ultimately achieve maximum dispersion according to this measure.

tional to time for high Stokes numbers. The proportionality in time is similar to the expression given by Hinze[33] for dispersion in a homogeneous turbulent flow, where the same dispersion function is equal to the product of time and particle turbulence intensity. Chein and Chung thus determined that particles of large Stokes number respond to the large-scale vortices as if they were simply homogeneous turbulence. Using this measure of dispersion, they furthermore observed the dispersion of particles at intermediate Stokes number exceeding that of the surrounding fluid. In their investigation of axisymmetric jets, Chung and Troutt[5] considered a similar mean-square dispersion function at different streamwise slices. The mean initial particle position was subtracted from the radial position of particles crossing the streamwise locations that were considered. They weighted this with the number of particles crossing radial subdivisions of the flow field. Based on this measurement, increased particle dispersion for intermediate Stokes number at different axial positions was demonstrated.

In each of the above studies, quantification of particle dispersion was based upon marker particles initially released from certain point sources. An alternative approach is to consider the instantaneous distribution of large numbers of particles throughout the flow field. Particle concentration can be treated as a near continuum quantity and
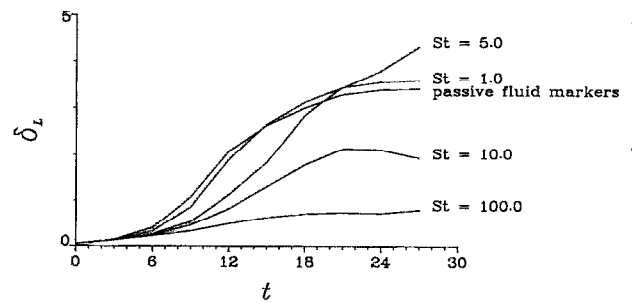
information on the dispersion of particles throughout the flow field obtained. In their experimental investigation of particle dispersion in a forced turbulent mixing layer, Lázaro and Lasheras[10] use a 0.9–0.1 level thickness to define the lateral spread of particles. The 0.9–0.1 level thickness is the difference between the cross-stream locations at which the particle concentration reaches 90% and 10% of the reference value, respectively,

$$\delta_L = y[c(y)/c_\infty = 0.9] - y[c(y)/c_\infty = 0.1].$$

Lázaro and Lasheras examine the streamwise variation of δ_L for various particle size diameters. Using this measure, they determine that intermediate size particles eventually disperse more effectively than the fluid itself. The dispersion of larger particles, however, remains below that of the passive fluid marker particles throughout the evolution of the flow.

For our temporally evolving mixing layer, δ_L is a function of time and Stokes number. The graph for the computed values of δ_L as a function of time (Fig. 10), shows the same trends as in the Lázaro and Lasheras experiments, with the values for intermediate Stokes numbers eventually exceeding those of passive fluid marker particles.

In Fig. 11, we plot the computed value of the 0.9–0.1 level thickness as a function of the Stokes number for times $t = 12$ and 18. We include the value attained for passive fluid particles as a dotted line. At each time in the simulation, the value of δ_L asymptotically approaches that of passive marker particles as the Stokes number decreases and the particles closely follow the motion of the fluid. By time 12, no particle size has undergone stronger dispersion than the fluid itself. However, by time 18 there is a range of intermediate Stokes numbers, for which particles disperse more effectively than the fluid. The maximum value for δ_L occurs roughly at a Stokes number of 2.5. This result of enhanced dispersion for St of $O(1)$ is in agreement with the earlier computations and measurements of other authors, as described above. From the above discussion of our results for St = 1.0 (Figs. 4 and 5), it is clear that the particle streaks play a major role in producing this enhanced dispersion.
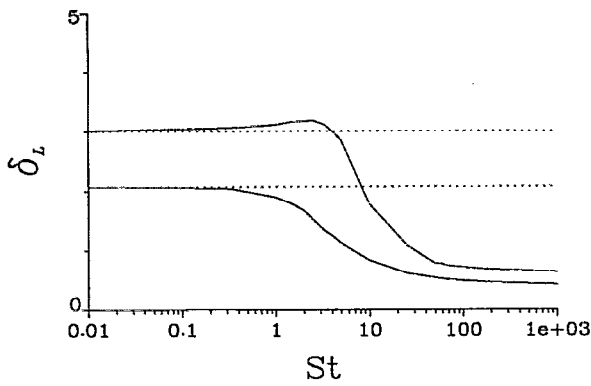
J. E. Martin and E. Meiburg

FIG. 11. 0.9–0.1 particle concentration level thickness as a function of St. ——: $t=12.0$; - - -: $t=18.0$. The value for passive fluid marker particles at each time is indicated by the dotted line. By time $t=18.0$, particles with St of $O(1)$ disperse more effectively than the surrounding fluid.

FIG. 13. Weighted particle displacement thickness as a function of St. ——: $t=12.0$; - - -: $t=18.0$; –.–.–; $t=30.0$. The value for passive fluid marker particles at each time is indicated by the dotted line. The moment of particles about the centerline of the mixing layer is maximized for St of $O(1)$.

For later times, the use of δ_L to quantify particle dispersion becomes problematic, as the streamwise-averaged concentration profile begins to exhibit pronounced peaks and the 10% and 90% levels are crossed repeatedly. A more precise measure of the *number* of particles entering the unseeded stream is given by the particle displacement thickness δ_d, where

$$\delta_d(t) = \int_0^\infty \frac{c(y,t=0.0) - c(y,t)}{c_\infty} \, dy = \int_{-\infty}^0 \frac{c(y,t)}{c_\infty} \, dy.$$

Here, δ_d effectively measures the number of particles that have crossed the centerline by equating it to the thickness of a region with the reference particle concentration. It is depicted as a function of the Stokes number in Fig. 12 for times $t=12$, 18, and 30. We recognize that, for all times, the largest number of particles in the lower stream occurs for the smallest particle Stokes numbers. The slight increase in the value of δ_d for very large Stokes numbers is due to the initial conditions for the particle velocities. Hence, the *number* of particles that crosses the midplane does not reach a maximum for intermediate values of the
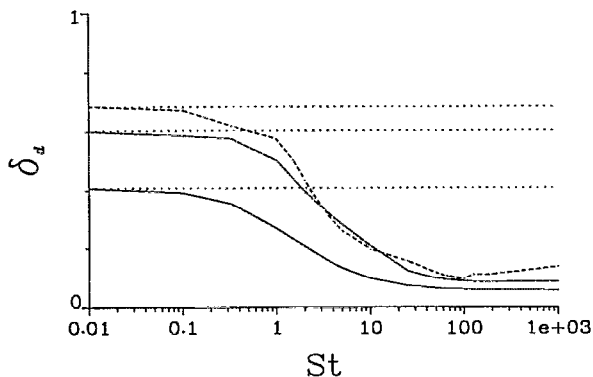
Stokes number. On the other hand, δ_d does not indicate how *far* the particles move, and it is therefore an incomplete indicator of dispersion. In many applications, it is most important that particles be dispersed a maximum distance. It is undesirable for a large number of particles to merely cross the centerline but not achieve a large cross-stream distance. By weighting the integrand of the particle displacement thickness with the absolute cross-stream distance from the centerline, we effectively compute the first moment of the particle concentration profile and obtain a quantity biased towards particles that have traveled greater distances into the unseeded stream. We call this quantity the weighted particle displacement thickness and denote it by δ_χ, where

$$\delta_\chi(t) = \int_{-\infty}^0 |y| \frac{c(y,t)}{c_\infty} \, dy.$$

Notice that, although formally having the dimension of length squared, δ_χ effectively gives the product of the number of particles that have crossed the centerline with the distance of their center of mass from the centerline. In Fig. 13, δ_χ is shown as a function of the Stokes number for times $t=12$, 18, and 30. This figure shows a clear maximum of the dispersion for intermediate Stokes numbers. Comparing δ_L with δ_χ at the later stages in the flow development, we see that the maximum in δ_χ is attained for somewhat smaller Stokes numbers. A graph of δ_χ as a function of time for a variety of Stokes numbers (Fig. 14), again shows that particles with Stokes number of $O(1)$ eventually are dispersed optimally.

FIG. 12. Particle displacement thickness as a function of St. ——: $t=12.0$; - - -: $t=18.0$; – – –: $t=30.0$. The value for passive fluid marker particles at each time is indicated by the dotted line. At each time, the number of particles reaching the unseeded stream is greatest for smallest St.
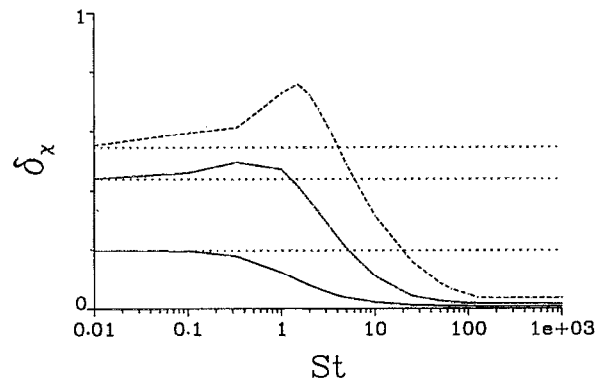
2. Particle velocity field

The particle concentration profiles, especially for St of $O(1)$ and greater, indicate the preference of particles to accumulate in narrow regions of the flow field. Both for St $=1.0$ and St $=10.0$ we noticed a tendency for particles to vacate regions of high vorticity and become more concentrated in narrow bands extending through the braid region.
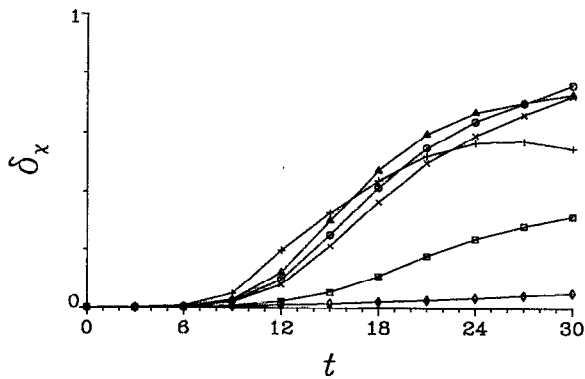
J. E. Martin and E. Meiburg   1125

FIG. 14. Evolution of the weighted particle displacement thickness: △, St=1.0; ○, St=1.5; ✕, St=2.0; □, St=10.0; ◇, St=100.0; +, passive fluid marker particles. The St=1.0 results are the first to exceed that of the surrounding fluid. Ultimately, by time t=30.0, particles with St slightly greater than one become dispersed optimally according to this measure.

FIG. 15. Regions of negative divergence of the particle velocity field superimposed on the overall particle concentration at time t=18.0 for St=1.5. Particles are directed into a single band of high particle accumulation which extends through the braid region, and forms much of the particle streaks.

The accumulation of these particles is significant because they eventually compose the particle streaks.

In order to more closely investigate the accumulation process, we compute a particle velocity field. As with the overall particle concentration contours, we subdivide the flow field into a number of rectangular bins. The velocities of all particles within each bin are then added, and the sum is divided by the bin's total number of particles. This gives us an average particle velocity for each bin. The particle velocity field need not be divergence free, i.e., particles may leave a region of the flow without the necessary simultaneous reintroduction of other particles to that region. We use a total of 500 000 particles and 12 800 bins for the computation of the particle velocity field.

Using the computed particle velocity fields, we determine the divergence at different times. We exclude from consideration bins containing less than 10 particles. When possible, we use a second-order central differencing scheme for calculating the derivatives. Otherwise, we use a more compact first-order stencil. For Stokes numbers much smaller than one, there is little evidence of nonzero divergence in the particle velocity field. However, for Stokes numbers of $O(1)$, we observe one region of strong negative divergence. Figure 15 contains contours of negative divergence (plotted at 10% increments of the maximum) for St=1.5 (the Stokes number which ultimately shows the overall maximum δ_χ). We superimpose the contours over the corresponding particle concentration field at time t=18. A single triangular region of strong negative divergence occurs in the stagnation point region of the flow. Elsewhere, positive divergence (not shown) is very weak. The contours of negative divergence surround the thin band of large particle accumulation extending through the braid region. Negative values of the divergence indicate convergence of particle velocity vectors. Particles in this region are directed into the band, resulting in the locally high particle concentration.

For larger Stokes number, two regions of strong negative divergence occur within the braid region. Figure 16
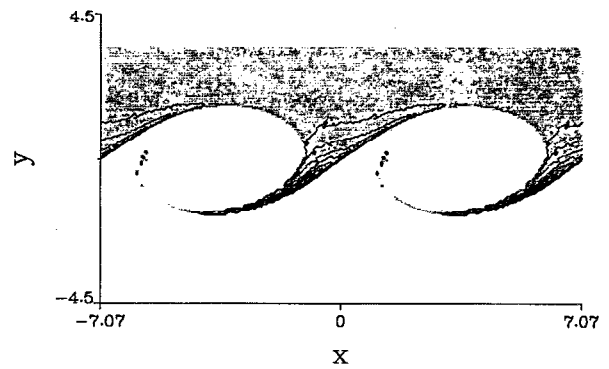
shows the contours of negative divergence for the Stokes number 10 simulation at the same time of t=18. The two regions are nearly parallel, and each of them is more confined than for St=1.5. These features of the particle velocity divergence field near the free stagnation point confirm the tendency of the particles to concentrate in high strain regions, as observed by other investigators. In particular, situations of particle accumulation were observed by Maxey,[34] as well as by Maxey and Corrsin[35] in a cellular velocity field, and by Fernández de la Mora and Riesco-Chueca[36] for potential flow fields. Maxey[34] remarked upon the accumulation of particles by considering a similar particle "flow field." He derived an analytical expression by using an approximation to the particle acceleration equation, accurate to first order in the Stokes number. Its divergence was found to be positive in regions of strong vorticity, or negative where the rate of strain is dominant. This suggested the accumulation of particles in regions of low vorticity or high strain. In the following, we will try to elucidate the particle accumulation mechanism in more detail by investigating a simple model of the flow field near the free-stagnation points.
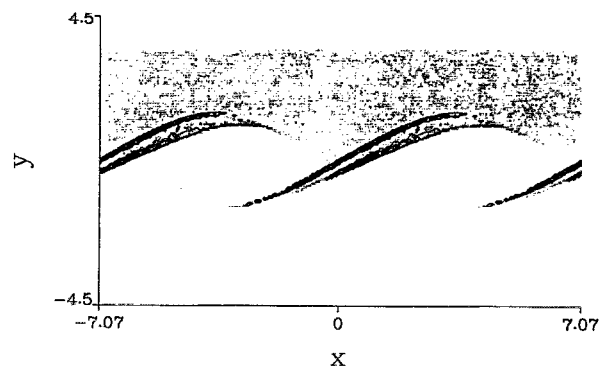

FIG. 16. Regions of negative divergence of the particle velocity field superimposed on the overall particle concentration at time t=18.0 for St=10.0. Two regions of negative divergence indicate the strong accumulation of particles into two narrow bands.

J. E. Martin and E. Meiburg

3. Stagnation point flow

The above discussion provides some insight into the formation and evolution of the streaks. Particles gather in the stagnation point region downstream of the vortex and then become stretched along the extensional streamline. We now focus our attention on this braid region where the particle velocity field was shown to have a negative divergence. In this region, the fluid velocity field can be modeled by the more simple stagnation point flow of the form

$$u=ax, \quad v=-ay, \tag{5}$$

with a being a positive constant. Morrison[37] has considered the collision of particles with an obstacle using the same stagnation point flow field as a model for flow near the obstacle's surface. In (5), x and y now represent a coordinate system whose axes are aligned with the directions of extensional and compressive strain. In full mixing layers, these directions change with time as the Kelvin–Helmholtz instability evolves. The particle acceleration in such a flow field is governed by the linear set of ordinary differential equations,

$$\frac{du_p}{dt}=\frac{1}{St}(ax_p-u_p),$$

$$\frac{dv_p}{dt}=-\frac{1}{St}(ay_p+v_p),$$

with solution given by

$$x_p=c_1e^{\lambda_1 t}+c_2e^{\lambda_2 t}, \tag{6}$$

$$y_p=c_3e^{\lambda_3 t}+c_4e^{\lambda_4 t}, \tag{7}$$

in which

$$\lambda_1=\frac{-1+\sqrt{1+4a\,St}}{2\,St}, \quad \lambda_2=\frac{-1-\sqrt{1+4a\,St}}{2\,St},$$

$$\lambda_3=\frac{-1+\sqrt{1-4a\,St}}{2\,St}, \quad \lambda_4=\frac{-1-\sqrt{1-4a\,St}}{2\,St},$$

and the coefficients c_1 through c_4 are determined through initial conditions. The envelopes of particle trajectories decay exponentially with t, but for $a\,St>1/4$ particles exhibit a nonmonotonic behavior. The amplitude of this oscillation decreases for increasing t. Its wavelength increases with increasing Stokes number.

The full mixing layer with large-scale vortices, can be modeled as a row of point vortices of strength κ separated by the wavelength of the mixing layer L. The velocity field for this arrangement is given by[38]

$$u=-\frac{\kappa}{2L}\frac{\sinh(2\pi y/L)}{\cosh(2\pi y/L)-\cos(2\pi x/L)},$$

$$v=\frac{\kappa}{2L}\frac{\sin(2\pi x/L)}{\cosh(2\pi y/L)-\cos(2\pi x/L)}.$$

By considering all the vorticity within each wavelength of the mixing layer as residing at the location of each point vortex, κ takes the value L. The strain rate a at the braid stagnation point between successive point vortices is then

given by $\pi/2L$. The critical Stokes number for the oscillations described above is $L/2\pi$. Although our wavelength is slightly larger than 2π, we illustrate the situation for $L=2\pi$. For the resulting $a=1/4$, we plot in Fig. 17 particle trajectories in the stagnation point flow field given by Eq. (5) for St=0.1, 1.0, and 10.0. We release particles at $-0.005<x<0.005$ and $y=1.0$. Initially, we assign the particle velocity equal to the fluid velocity at the particle's location. The dashed lines indicate the streamlines of the flow. For St=0.1 [Fig. 18(a)], particles spread from the stagnation point as they follow the motion of the fluid. For St=1.0, however, there is an optimal focusing of particles towards the stagnation point of the flow. The particles converge towards the dividing streamline at optimum speed. Consequently, there is a rapid buildup of particles along the stagnation streamline. This results in the single line of heavy particle accumulation which we observe in the full mixing layer at St $O(1)$. This focusing of particles along the stagnation streamline, furthermore accounts for the strong region of negative divergence in the particle velocity field at St $O(1)$ (Fig. 15).

The optimal buildup of particles at St $O(1)$ allows large numbers of particles to be, in turn, accelerated by the overall extensional strain field of the full mixing layer. This produces the high accumulation streaks which extend well into the slower stream, and it provides additional quantitative support for the preferential dispersion of particles at Stokes number near unity observed in previous investigations.

Figure 17(c) shows the trajectories of particles for a Stokes number of 10.0. For this Stokes number, oscillations of the particles about the stagnation streamline occur. Particles have enough inertia to cross the stagnation streamline, but are forced back across the streamline due to the opposing flow. As Eq. (7) shows, the amplitude of this oscillation will decrease with time and particles will eventually converge to $y=0$ for large times. Because the residence time is large during particle reversal, one can anticipate the formation of two regions of high particle concentration near the dividing streamline, one occurring at the maximum and one at the minimum of the oscillation. By releasing large numbers of particles into this flow field, two such regions of larger particle accumulation are observed [Fig. 17(d)]. As pointed out earlier, the wavelength of the oscillations in the y_p trajectory solution increases with increasing Stokes number. Therefore, the possibility for the formation of multiple, high density lines for Stokes numbers much greater than 10.0 becomes limited.

In light of these findings, we return and examine the full mixing layer calculation for Stokes numbers 1.0 and 10.0. In Fig. 18, we magnify the region surrounding the stagnation point at time $t=15.0$ for each case, plotting every particle occurrence. For St=1.0, large particle accumulation occurs in a single band delineated by the stagnation streamline. For the St=10.0 case however, two lines of increased particle accumulation become evident. These two lines account for the two regions of negative particle divergence we observe in the particle velocity field for this Stokes number (Fig. 16). The lines of higher particle ac-
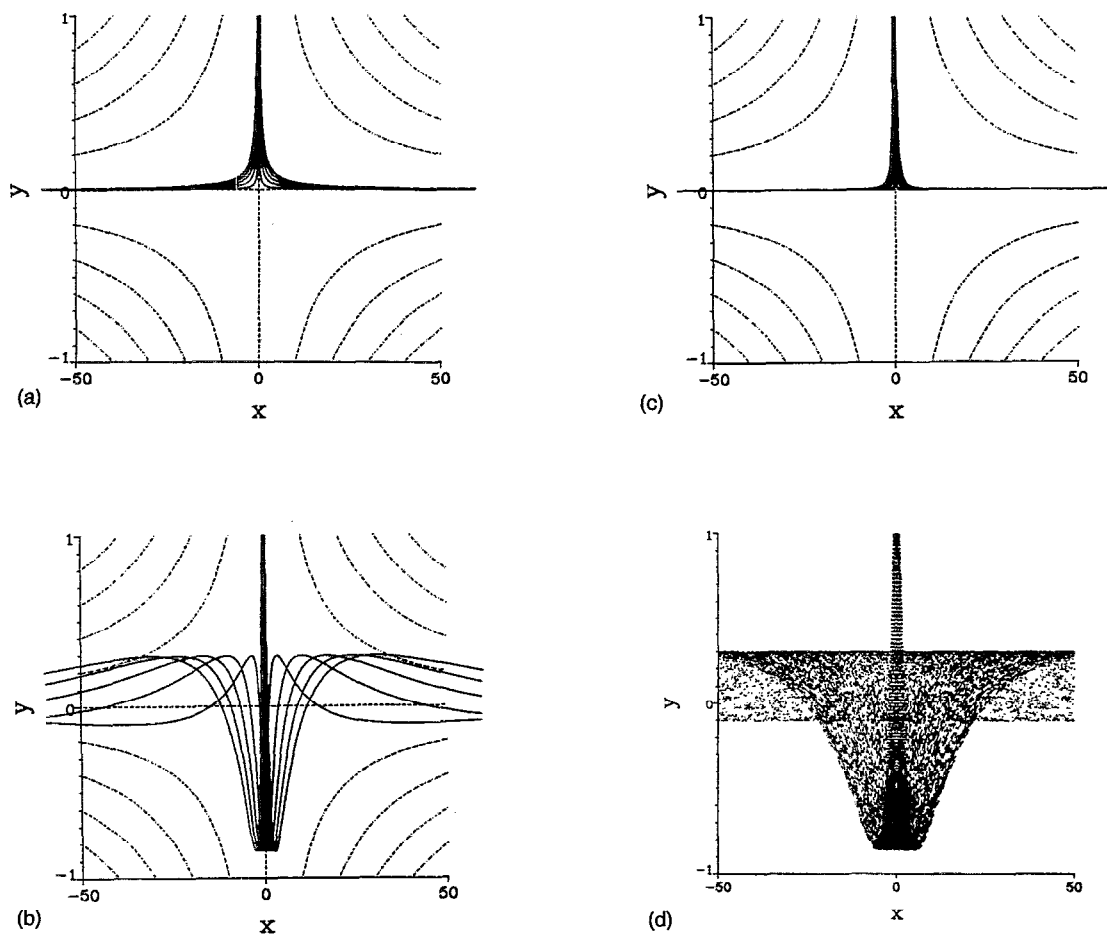
FIG. 17. Streamlines ($\cdots$) and particle trajectories (——) in a simple stagnation point flow: (a) St=0.1, (b) St=1.0, and (c) St=10.0. For smaller values of St, the particles closely follow the streamlines, resulting in a weak accumulation of particles. The rate of particle accumulation along the dividing streamline becomes optimal for St=1.0. For higher value of St, the particle trajectory solution becomes underdamped; we observe an overshoot of the particles and subsequent oscillation, resulting in the formation of two bands of large particle accumulation. (d) Resulting particle locations for 36 000 particles introduced into the stagnation point flow for St=10.0. Two bands of large particle accumulation occur, at the peak and the trough of the particle oscillation.

cumulation and regions of negative divergence occur at the peak and trough of particle oscillation. Figure 19 shows the beginning oscillations in some of the trajectories, for particles shown in Fig. 18(b).

4. Effect of vortex pairing

It is well known that subharmonic vortex pairing represents the dominant mechanism for mixing layer growth.[4] Hence, it is important to examine how the scenario for particle dispersion described above becomes modified in the presence of subharmonic perturbations that lead to vortex pairing. Chein and Chung[6] concluded from their investigation that particle dispersion is stronger during a vortex pairing event than before or afterwards. Kiger and Lasheras[11] found that the vortex pairing mechanism leads to a more homogeneous distribution of their polydispersed particles.

In the following, we will extend our detailed numerical simulations to flow fields containing both a fundamental and a subharmonic perturbation. For this purpose, we double the length of our control volume. The fundamental

wave is introduced in the same way and with the same amplitude as above. The subharmonic wave, which initially is of the same amplitude as the basic wave, also affects the circulation of the blobs. Its phase is such that its amplitude reaches a maximum midway between the two evolving vortices. In this way, the two equally strong vortices will proceed towards a pairing event rather than a tearing process. In the following, we focus on the evolution of the flow field for the St=1 case. Figure 20 contains the particle locations superimposed over the vorticity contours of the continuous phase. Plotted are 4725 of the 450 000 particles followed in the simulation. By time $t=18$, [Fig. 20(a)] near circular vortices form in the continuous fluid phase. Due to the subharmonic perturbation, these vortices become displaced above and below the mixing layer as they proceed towards pairing. The deformation field between successive vortices again leads to the formation of particle streaks entering the unseeded stream. It is important to realize that the strain rate is stronger in the region between the pairing vortices than it is in the region between successive vortex pairs. Correspondingly, the streaks between pairing vortices un-

J. E. Martin and E. Meiburg
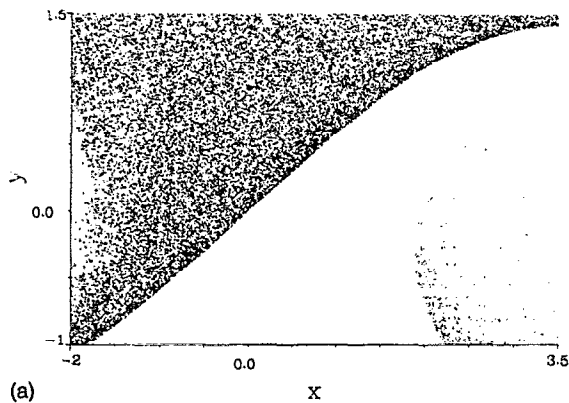
(a)
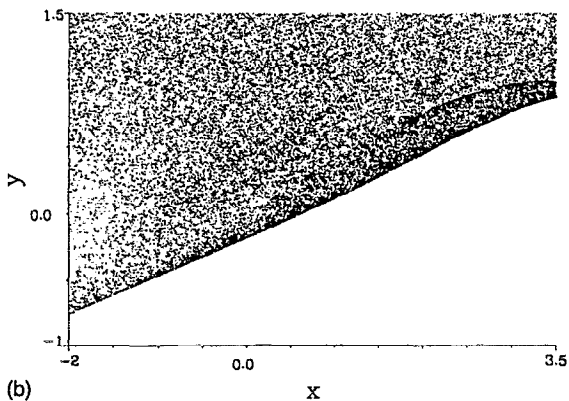
(b)

FIG. 18. Magnification of the stagnation point region of the full mixing layer at time $t=15.0$ for St equal to (a) 1.0 and (b) 10.0. For St=1.0, particles accumulate in a single band delineated by the stagnation streamline, whereas for St=10.0, two lines of increased particle accumulation in the area surrounding the stagnation point become evident.
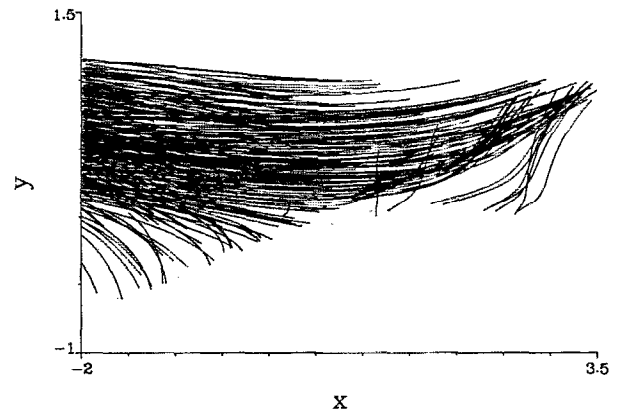

FIG. 19. Trajectories of particles within magnified region whose final position is given in Fig. 18(b), St=10.0. The beginning oscillatory behavior of the particles appears in the trajectories at the rightmost portion of the figure.

dergo a different evolution from those in between vortex pairs. The streamwise-averaged concentration plot now shows four well-developed local maxima, which can be related to the evolving streaks.

By time $t=30$, the streaks have wrapped entirely around the vortex pairs. Those streaks in between pairing vortices undergo a more intensive stretching, which leads to their more rapid depletion of particles. The shape of the depleted region around the vortex pair reflects not only the instantaneous centrifugal action by the vortices, but also a time integration effect: the remnants of the original, but now strongly deformed regions of depletion around each individual vortex are still clearly visible.

At time $t=54$, we stop the pairing calculation. The folding and stretching of the particle streaks, cf. also Wen et al.,[13] continues and leads to the formation of lobe-like structures which resemble those observed in the study of chaotic mixing layer dynamics by Meiburg et al.[29] The overall shape of the particle concentration profile begins to look quite similar to that for the fundamental wave only

case, with well-developed spikes above and below the plane of the vortex pairs.

The particle dispersion for the perturbed mixing layer undergoing pairing can be quantified in a similar fashion to the case of the fundamental wave only. In Fig. 21, we plot δ_χ as a function of the Stokes number for times $t=12$, 30, and 54. According to this measure, an intermediate range of Stokes numbers again is dispersed more effectively than fluid elements. By time 54, the maximum in δ_χ occurs roughly at a Stokes number slightly greater than one, as in the fundamental wave only case.

Figure 22 shows δ_χ as a function of time for different values of the Stokes number. We find that, compared to the fundamental wave only case, it now takes considerably longer for the optimally dispersed heavy particles to exceed the dispersion of the fluid elements. There appear to be two main differences between the evolution of the basic case and the subharmonic case. The first of these concerns the extensional strain field. In the case without pairing, the extensional strain field between successive vortices acts in approximately the same direction for all times, thereby continuously directing large numbers of particles across the centerline of the mixing layer. If vortex pairing takes place, on the other hand, the strain field in between pairing vortices undergoes a continual reorientation in space. Particles are no longer necessarily directed towards the unseeded stream. On the other hand, the rotating motion of the pairing vortices around each other lets them sweep out a much larger part of the flow field, so that they can capture and eject into the unseeded stream a larger number of particles. The combined effect of these two mechanisms is an enhanced dispersion of particles (Fig. 23), although intermediate size particles do not necessarily experience stronger dispersion than fluid particles, as was seen in Fig. 22.

IV. SUMMARY AND CONCLUSIONS

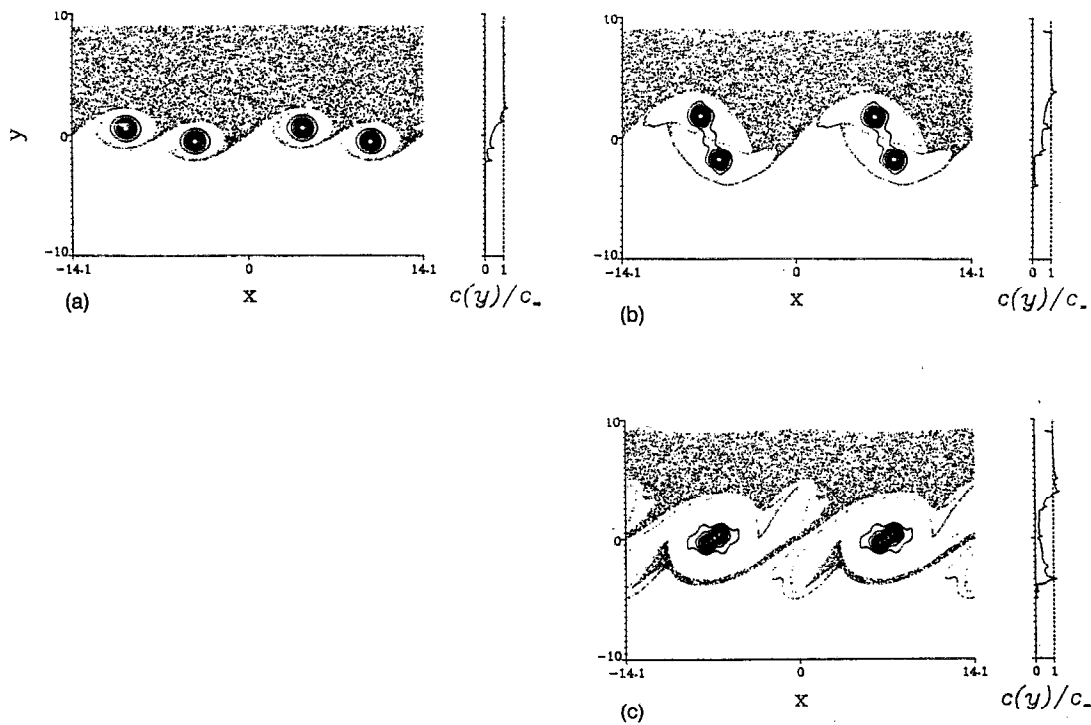We have presented detailed computational results for the dispersion of heavy particles in transitional mixing lay-

FIG. 20. Vorticity contours with particle positions superimposed for St=1.0 at times (a) t=18.0, (b) t=30.0, and (c) t=54.0 for the plane mixing layer under additional, equal-amplitude, subharmonic perturbation. By time t=18.0, particle streaks surround the pairing vortices. By time t=30.0, particle streaks between pairing vortices become depleted, while particle streaks between vortex pairs become extended. Each vortex sweeps out ear-shaped regions devoid of particles.

ers forced at both the fundamental and the subharmonic frequencies. Our results confirm the observations of other investigators that streaks of particles forming in the braid region between successive vortices dominate the dispersion process. These streaks are closely aligned with the extensional direction of the stagnation point flow field. A scaling argument, based on the idealization of the spatially periodic mixing layer as a row of point vortices, shows that the formation of these concentrated particle streaks proceeds

with optimum efficiency for St$\simeq$1, in agreement with experimental and numerical observations of preferential particle dispersion at Stokes numbers of order unity. The stagnation point flow field model furthermore predicts the formation of *two* bands of high particle concentrations for Stokes numbers somewhat larger than one, which is con-
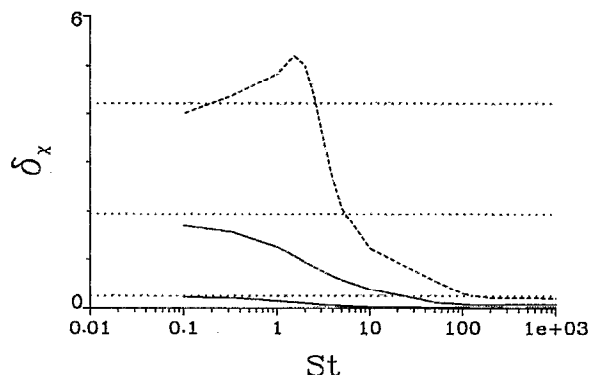

FIG. 21. Weighted particle displacement thickness for a plane mixing layer under additional, equal amplitude, subharmonic perturbation. ———: t=12.0; - - -: t=30.0; — — —: t=54.0. δ_χ for passive fluid marker particles at each time is indicated by the dotted line. In contrast to the fundamental wave only case, by time 30.0, no particle Stokes number disperses more effectively than the surrounding fluid. Eventually, by time t=54.0, a range of St of $O(1)$ achieve dispersion in excess of the surrounding fluid.
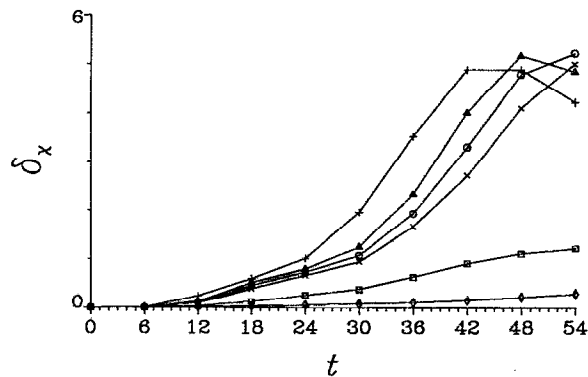

FIG. 22. Evolution of the weighted particle displacement thickness for a plane mixing layer under additional, equal amplitude subharmonic perturbation: $\triangle$, St=1.0; $\bigcirc$, St=1.5; $\times$, St=2.0; $\square$, St=10.0; $\Diamond$, St=100.0; +, passive fluid marker particles. δ_χ is greatest for passive fluid marker particles roughly until time t=46.0. The extensional strain field undergoes a continual reorientation for the mixing layer undergoing pairing. Therefore, the mechanisms by which particles accumulate at St of $O(1)$ are less efficient than those in a mixing layer without pairing. By time t=54.0, the vortices have neared completion of pairing, and the particles with St slightly greater than one achieve maximum dispersion.
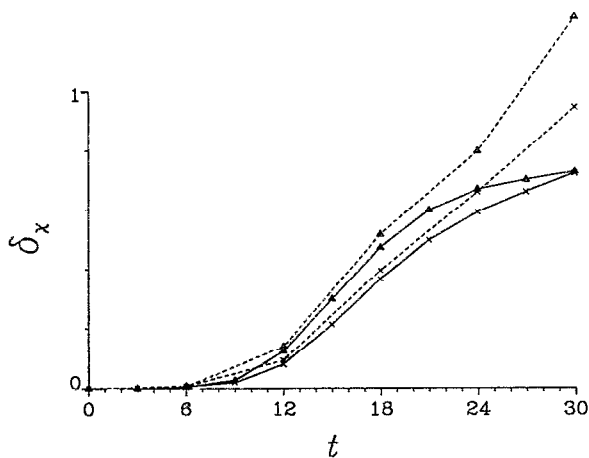
FIG. 23. Evolution of the weighted particle displacement thickness for the mixing layer under fundamental only (———) and under additional subharmonic (- - -) perturbation: $\triangle$, St=1.0; $\times$, St=2.0. For each St, dispersion of particles is greater at all times for the mixing layer undergoing vortex pairing.

firmed by the concentration field and the divergence of the particle velocity field in the full mixing layer simulation for St=10. Both the model and the full simulation show oscillatory particle trajectories at this Stokes number.

We quantify the particle dispersion as a function of time and St by means of two different integral scales. The first one, which represents a measure of the *number* of particles that have crossed the mixing layer, does not exhibit a maximum for intermediate Stokes numbers. However, if we weight with the *distance* that the particles have traveled into the unseeded stream, we do find an optimum for intermediate values of the Stokes number.

Our calculations furthermore allow us to trace back in time the locations of those particles that experience ejection into the unseeded stream. We find that these particles originate in inclined narrow bands that initially stretch from the braid region into the seeded free stream. The fact that these regions are very localized indicates that particle dispersion in an experiment can be optimized by phase-coupling the injection device with the forcing signal for the continuous phase.

When we introduce a subharmonic perturbation into our flow field as well, we find that the region in between pairing vortices evolves quite differently from the region in between vortex pairs. The strain field in between pairing vortices increases in strength, which leads to a rapid ejection of particles from this region. However, since this local strain field also undergoes a continuous rotation in time, this ejection does not necessarily enhance the flux of particles into the unseeded stream. On the other hand, during the pairing process the vortices spiral around each other, thereby sweeping a much larger region of the flow field than in the case without pairing. This effect leads to increased overall particle dispersion in the presence of a subharmonic wave.

The present investigation draws attention to the importance of the braid region in the particle dispersion pro-

cess. It is well known that concentrated and strained counterrotating streamwise vortices form in this region.[39–42] Consequently, these can be expected to play a significant role in the particle dispersion by a three-dimensional evolving mixing layer. This issue is currently addressed in a separate investigation.

ACKNOWLEDGMENTS

[1] K. D. Squires and J. K. Eaton, "Measurements of particle dispersion obtained from direct numerical simulations of isotropic turbulence," J. Fluid Mech. **226**, 1 (1991).

[2] C. T. Crowe, R. A. Gore, and T. R. Troutt, "Particle dispersion by coherent structures in free shear flows," Part. Sci. Tech. **3**, 149 (1985).

[3] G. L. Brown and A. Roshko, "On density effects and large structure in turbulent mixing layers," J. Fluid Mech. **64**, 775 (1974).

[4] C. D. Winant and F. K. Browand, "Vortex pairing: the mechanism of turbulent mixing-layer growth at moderate Reynolds number," J. Fluid Mech. **63**, 237 (1974).

[5] J. N. Chung and T. R. Troutt, "Simulation of particle dispersion in an axisymmetric jet," J. Fluid Mech. **186**, 199 (1988).

[6] R. Chein and J. N. Chung, "Effects of vortex pairing on particle dispersion in turbulent shear flows," Int. J. Multiphase Flow **13**, 785 (1987).

[7] C. T. Crowe, J. N. Chung, and T. R. Troutt, "Particle dispersion by organized turbulent structures," in *Particulate Two-Phase Flow*, edited by M. C. Roco (Butterworth–Heinemann, Stoneham, MA, 1993).

[8] B. J. Lázaro and J. C. Lasheras, "Particle dispersion in a turbulent, plane, free shear layer," Phys. Fluids A **1**, 1035 (1989).

[9] B. J. Lázaro and J. C. Lasheras, "Particle dispersion in the developing free shear layer. Part 1, unforced flow," J. Fluid Mech. **235**, 143 (1992).

[10] B. J. Lázaro and J. C. Lasheras, "Particle dispersion in the developing free shear layer. Part 2, forced flow," J. Fluid Mech. **235**, 179 (1992).

[11] K. T. Kiger and J. C. Lasheras, "Vortex pairing and particle dispersion in a turbulent free shear layer," preprint (1993).

[12] E. K. Longmire and J. K. Eaton, "Structure and control of a particle-laden round jet," J. Fluid Mech. **236**, 217 (1992).

[13] F. Wen, N. Kamalu, J. N. Chung, C. T. Crowe, and T. R. Troutt, "Particle dispersion by vortex structures in plane mixing layers," ASME J. Fluids Eng. **114**, 657 (1992).

[14] A. M. Gañán-Calvo and J. C. Lasheras, "The dynamics and mixing of small spherical particles in a plane, free shear layer," Phys. Fluids A **3**, 1207 (1991).

[15] J. T. Stuart, "On finite amplitude oscillations in laminar mixing layers," J. Fluid Mech. **29**, 417 (1967).

[16] K.-K. Tio, A. Liñán, J. C. Lasheras, and A. M. Gañán-Calvo, "On the dynamics of buoyant and heavy particles in a periodic Stuart vortex flow," J. Fluid Mech. **254**, 671 (1993).

[17] K.-K. Tio, A. M. Gañán-Calvo, and J. C. Lasheras, "The dynamics of small, heavy, rigid spherical particles in a periodic Stuart vortex flow," Phys. Fluids A **5**, 1679 (1993).

[18] K.-K. Tio and J. C. Lasheras, "The dynamics of a small spherical particle in a modified Rankine vortex flow under the influence of gravity," Phys. Fluids A (in press).

[19] N. Raju and E. Meiburg, "The accumulation and dispersion of heavy particles in forced two-dimensional mixing layers. Part 2: The effect of gravity," preprint (1993).

[20] A. Leonard, "Vortex methods for flow simulation," J. Comput. Phys. **37**, 289 (1980).

[21] G. K. Batchelor, *An Introduction to Fluid Mechanics* (Cambridge University Press, Cambridge, 1967).

Phys. Fluids, Vol. 6, No. 3, March 1994

J. E. Martin and E. Meiburg   1131

[22]Y. Nakamura, A. Leonard, and P. Spalart, "Vortex simulation of an inviscid shear layer," AIAA Paper No. 82-0948, 1982.

[23]A. Michalke, "On the inviscid instability of the hyperbolic-tangent velocity profile," J. Fluid Mech. **19**, 543 (1964).

[24]M. R. Maxey and J. J. Riley, "Equation of motion for a small rigid sphere in a nonuniform flow," Phys. Fluids **26**, 883 (1983).

[25]S. Balachandar and M. R. Maxey, "Methods for evaluating fluid velocities in spectral simulations of turbulence," J. Comput. Phys. **79**, 96 (1989).

[26]F. K. Browand, H. Nassef, and P. R. Spalart, "The motion of heavy particles in a turbulent boundary layer: problem formulation and preliminary statistical results," USCAE Report No. 148, 1991.

[27]R. L. Burden and J. D. Faires, *Numerical Analysis*, 3rd ed. (Prindle, Weber, and Schmidt, Boston, 1978).

[28]V. Rom-Kedar, A. Leonard, and S. Wiggins, "An analytical study of transport, mixing and chaos in an unsteady vortical flow," J. Fluid Mech. **214**, 347 (1990).

[29]E. Meiburg, N. Raju, and P. K. Newton, "The mixing transition: dynamical and kinematic considerations," preprint (1993).

[30]L.-P. Wang, "Dispersion of particles injected nonuniformly in a mixing layer," Phys. Fluids A **4**, 1599 (1992).

[31]G. K. Batchelor, "Diffusion in free turbulent shear flows," J. Fluid Mech. **3**, 67 (1956).

[32]R. Chein and J. N. Chung, "Simulation of particle dispersion in a two-dimensional mixing layer," AIChE J. **34**, 946 (1988).

[33]J. O. Hinze, *Turbulence*, 2nd ed. (McGraw-Hill, New York, 1975).

[34]M. R. Maxey, "The motion of small spherical particles in a cellular flow field," Phys. Fluids **30**, 1915 (1987).

[35]M. R. Maxey and S. Corrsin, "Gravitational settling of aerosol particles in randomly oriented cellular flow fields," J. Atmos. Sci. **43**, 1112 (1986).

[36]J. Fernández De La Mora and P. Riesco-Chueca, "Aerodynamic focusing of particles in a carrier gas," J. Fluid Mech. **195**, 1 (1988).

[37]F. A. Morrison, "Inertial impaction in stagnation flow," Aerosol Sci. **5**, 241 (1974).

[38]H. Lamb, *Hydrodynamics*, 6th ed. (Cambridge University Press, Cambridge, 1932).

[39]S. J. Lin and G. M. Corcos, "The mixing layer: deterministic models of a turbulent flow. Part 3: The effect of plane strain on the dynamics of streamwise vortices," J. Fluid Mech. **141**, 139 (1984).

[40]L. P. Bernal and A. Roshko, "Streamwise vortex structures in plane mixing layers," J. Fluid Mech. **170**, 499 (1986).

[41]W. T. Ashurst and E. Meiburg, "Three-dimensional shear layers via vortex dynamics," J. Fluid Mech. **189**, 87 (1988).

[42]J. C. Lasheras and H. Choi, "Three-dimensional instability of a plane, free shear layer: an experimental study of the formation and evolution of streamwise vortices," J. Fluid Mech. **189**, 53 (1988).